

# Validity of the Bruggeman relation for porous electrodes

Ding-Wen Chung<sup>1</sup>, Martin Ebner<sup>2</sup>, David R Ely<sup>1</sup>, Vanessa Wood<sup>2</sup>  
and R Edwin García<sup>1</sup>

<sup>1</sup> School of Materials Engineering, Purdue University, West Lafayette, IN, USA

<sup>2</sup> Department of Information Technology and Electrical Engineering, ETH Zurich, Zurich, Switzerland

Received 13 February 2013, in final form 20 April 2013

Published 8 October 2013

Online at [stacks.iop.org/MSMSE/21/074009](http://stacks.iop.org/MSMSE/21/074009)

## Abstract

The ability to engineer electrode microstructures to increase power and energy densities is critical to the development of high-energy density lithium-ion batteries. Because high tortuosities in porous electrodes are linked to lower delivered energy and power densities, in this paper, we experimentally and computationally study tortuosity and consider possible approaches to decrease it. We investigate the effect of electrode processing on the tortuosity of in-house fabricated porous electrodes, using three-dimensionally reconstructed microstructures obtained by synchrotron x-ray tomography. Computer-generated electrodes are used to understand the experimental findings and assess the impact of particle size distribution and particle packing on tortuosity and reactive area density. We highlight the limitations and tradeoffs of reducing tortuosity and develop a practical set of guidelines for active material manufacture and electrode preparation.

(Some figures may appear in colour only in the online journal)

## 1. Introduction

The higher rate capability and better cycle life of lithium-ion batteries with porous electrode microstructures has enabled its worldwide implementation in consumer electronics, electric vehicles and stationary energy storage [1]. Fundamentally, the theoretical description of the galvanostatic cycling process is summarized in terms of the well-established porous electrode theory [2–13]. Here, the macroscopic porosity and average particle size embody the relevant macroscopic microstructural parameters of the porous electrode, specify the power and energy densities and contribute to the polarization losses. Based on these quantities, the tortuosity is described by the well-known Bruggeman relation:

$$\tau = \frac{1}{\epsilon^{1/2}}, \quad (1)$$

**Table 1.** List of symbols.

Symbol	Name
$D$	Electrolyte lithium diffusivity
$D_m$	Macroscopic lithium diffusivity
$L$	Electrode thickness
$P$	Compaction stress
$S_A$	Surface roughness coefficient
$a$	Exposed area of active material per unit volume
$f_v$	Weight fraction of inactive additives
$l$	Ion diffusion length
$\bar{r}$	Average particle radius
$\epsilon_o$	Active material porosity
$\epsilon_T$	Total electrode porosity
$\epsilon_v$	Inactive material porosity
$\sigma_i$	Local polydispersity of neighboring particles
$\sigma_{\max}$	Maximum neighbor particles polydispersity
$\sigma_r$	Electrode particle size polydispersity
$\tau_o$	Active material tortuosity
$\tau_T$	Total electrode tortuosity
$\tau_v$	Inactive material tortuosity
$\chi$	Degree of crystallinity

where  $\tau$  is the tortuosity and  $\epsilon$  is the porosity. Similarly, the density of electrochemically active reaction sites,  $a$ , is given by the area per unit volume of active material, i.e.,

$$a = \frac{3(1 - \epsilon)}{\bar{r}}, \quad (2)$$

where  $\bar{r}$  is the average particle radius.

Historically, the energy and power density of a battery have been improved by minimizing undesired microstructural induced polarization losses such as interfacial, concentration and ohmic. Tortuous transport paths result in a higher macroscopic ohmic resistance, which in turn hinders the delivered energy and power density [14–17].

In agreement with Wheeler and co-workers [18, 19], Harris and co-workers [20] and Vijayaraghavan *et al* [21], tortuosity is correlated with the macroscopic diffusivity  $D_m$  through the expression [22, 23]:

$$D_m = D \frac{\epsilon}{\tau}, \quad (3)$$

where  $D$  is the ion diffusivity in the electrolyte. Geometrically, tortuosity is commonly defined as the ratio of the average ion diffusion length to the electrode thickness,  $\tau = l/L$ , where  $l$  is the ion diffusion length across the electrode and  $L$  is the electrode thickness [24]. Symbols and properties used in this paper are summarized in table 1.

For more than 50 years, porous electrode theory has relied on the use of equation (1), as proposed originally by Bruggeman to estimate the electrode tortuosity [2, 3, 25]. However, recent experimental results indicate that the complexity of the porous electrode microstructure induces tortuosity values that greatly deviate from the classical Bruggeman ideal [15, 26–28]. Ferguson and Bazant elaborate further on this, and highlight that lower and upper bounds to tortuosity exist in porous media, ranging from anisotropic, Weiner, to isotropic, Hashin–Shtrikman bounds [29–32]. In this context, Thorat and Wheeler defined a generalized relation,  $\tau = A/\epsilon^B$ , to describe experimentally measured tortuosities [18].

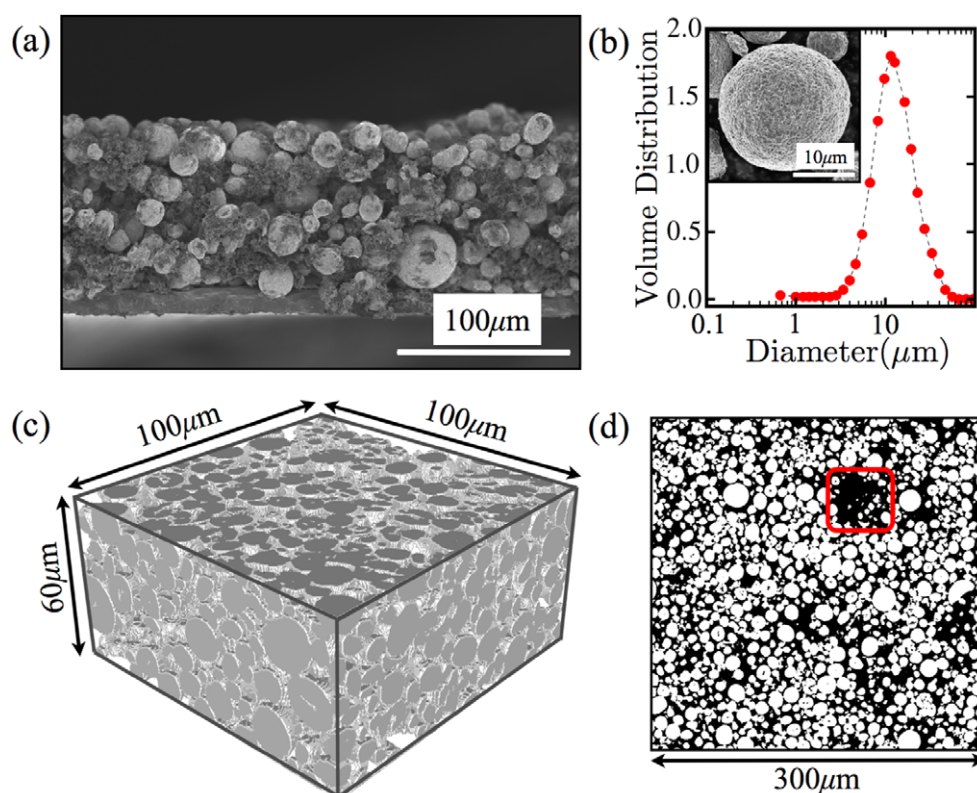


**Figure 1.** (a) SEM micrograph of a porous electrode showing a mixture of  $\text{LiNi}_{1/3}\text{Mn}_{1/3}\text{Co}_{1/3}\text{O}_2$  particles, carbon black and polyvinylidene fluoride binder. (b) Corresponding lognormal particle size distribution measured by laser diffraction. The inset shows an SEM micrograph detailing its spherical morphology. (c) Three-dimensional rendering of an electrode microstructure. (d) Cross-section of electrode tomograph showing a region of spatial nonuniformity.

Shearing and Harris used x-ray tomography to analyze tortuosity homogeneity [20, 33], and found that microstructural variations across the electrode can locally increase the tortuosity by a factor of three. Similarly, Stephenson and Wheeler combine focused ion beam scanning electron microscopy (FIB-SEM) data with a three-dimensional microstructural correlation model to predict electrode tortuosity semi-quantitatively [19].

Numerically, Gupta, Sastry and Shyy report that the effective transport properties deviate from the Bruggeman estimate due to the randomness of possible configuration arrangements in particle packing [34]. Desilvestro and co-workers and White and co-workers analyzed the tortuosity anisotropy in crystalline structures and showed that tortuosity correlates strongly with the crystallographic orientation of the unit cell [35, 36].

In spite of the great progress in understanding the effects of microstructure on the macroscopic tortuosity of porous electrodes, correlations and guidelines between active particle size distribution and electrode processing and microstructural properties remain unavailable. In this paper, the effects of different processing variables on tortuosity are analyzed using experimentally fabricated electrodes (see figure 1). Computer-generated electrodes are then used to explain the observed microstructural properties of the experimental electrodes. Finally, potential microstructures with lower tortuosities and higher reaction site densities are proposed.

We adopt the following nomenclature to describe the porous electrode, which is composed of a micron-scale active material and inactive components including a nanoscale carbon black and a polymer binder. The total porosity of the electrode is given by  $\epsilon_T = \epsilon_o \epsilon_v$ , where  $\epsilon_o$  is the porosity of active material, which can be extracted from the tomography or numerical data,  $\epsilon_v$  is the porosity of the nanoscale inert material in the pore space left by the active material, and is calculated from weight percentage ratios and densities of electrode constituents.

Similarly, the different components of the electrode contribute to the tortuosity of the system [18–20, 33, 37]. Recently, García and co-workers developed an analytical relation that combines the effect of active phase tortuosity,  $\tau_o$ , and inactive material tortuosity,  $\tau_v$ , from inactive components [21]:

$$\tau_T = \tau_o \tau_v. \quad (4)$$

The tortuosity of active material,  $\tau_o$ , can be extracted from tomography data. However, because the inactive phase cannot be resolved through x-ray tomography, the nanoscale tortuosity created by the inactive materials residing in the pore space is not experimentally determined. We assume that the inert material uniformly fills the pores between the active particles, which is supported by SEM images of the experimental electrodes, showing carbon black uniformly populating the space between the active particles (figure 1(a)). Assuming validity of the Bruggeman relation for this phase, the inactive phase tortuosity is described as  $\tau_v = \epsilon_v^{-1/2}$ . To assess the validity of the Bruggeman relation for porous electrodes,  $\tau_o = \epsilon_o^{-1/2}$ , we study both the active material alone using no assumptions and together with the contribution of inactive phases under the mentioned assumptions,  $\tau_T = \epsilon_T^{-1/2}$ . Effects such as particle morphological anisotropy are not considered in this analysis.

## 2. Experimental setup

In this study, we utilize experimental data from [38]. Spherical  $\text{LiNi}_{1/3}\text{Mn}_{1/3}\text{Co}_{1/3}\text{O}_2$  (BC-618K from 3M Co., St Paul, MN, USA) was selected due to its highly spherical particle morphology (figure 1(b)). The particle size was found to match a lognormal distribution where the average radius is approximately  $6 \mu\text{m}$  with a polydispersity of  $\sigma_r = 0.4\bar{r}$ .

Sixteen electrodes with a range of inactive materials and states of compaction were prepared. Varying weight ratios (96:2:2, 94:3:3, 92:4:4 and 90:5:5) of spherical  $\text{LiNi}_{1/3}\text{Mn}_{1/3}\text{Co}_{1/3}\text{O}_2$ , nanometer-scale carbon black (Super C65 from TIMCAL Ltd, Bodio, Switzerland) and PVDF binder (Kynar 761 from Arkema, Philadelphia, PA, USA) were dissolved in *N*-methyl pyrrolidone solvent (NMP biotech grade from Sigma-Aldrich Chemie GmbH, Buchs, Switzerland) and then dispersed using a high shear dispenser. The resulting slurry was subsequently rested on a roller bench for up to 3 h to remove bubbles, cast onto  $12 \mu\text{m}$  thick aluminum foil using a  $200 \mu\text{m}$  notch bar, and dried under vacuum at  $80^\circ\text{C}$  for 8 h. Electrodes with a diameter of 13 mm were punched out with a proprietary puncher, and then compressed at room temperature during six cycles with increasing pressure up to 0.3, 0.6 and 2 kbar in a proprietary calendaring machine.

Large volume, synchrotron x-ray tomography as well as electrochemical cycling data for each of these electrodes are available in [38]. A representative three-dimensional rendering of an electrode microstructure is shown. We note that despite careful electrode preparation, some cross-sections in the reconstructed microstructure show empty areas (see figure 1(d)), possibly from suboptimal slurry mixing.

**Table 2.** DEM simulation parameters [48–50]. A Hooke's law contact model with a damping contribution was used to describe both the normal and tangential contact mechanics of particles during compaction.

Name	Value	Units
Damping coefficient	$1.81 \times 10^{-5}$	—
Density of active particles	4750	$\text{kg m}^{-3}$
Dynamic coefficient of friction	0.15	—
Poisson ratio of active particles	0.3	—
Static coefficient of friction	0.25	—
Young's modulus of active particles	200	GPa
Young's modulus of compaction wall	180	GPa

### 3. Numerical setup

Numerical representations of three-dimensional porous electrode microstructures were generated by inserting particles with a specific size distribution into a simulation domain of fixed dimensions. The porosity was defined through a discrete element method (DEM) package, ESyS-Particle [39]. The electrode was compacted to a specified porosity where the normal and rotational particle contact mechanics were defined through Hooke's law with a damping factor model [39]. Utilized simulation parameters are summarized in table 2. To generate electrodes with spatial inhomogeneities as highlighted in figure 1(d), a second population of particles, i.e. a carbon black aggregate phase not observable through x-ray tomography, was added to the simulation domain. The additional 10%, experimentally observed, void fraction imposed additional constraints on the packing of the active material particle phase during DEM electrode compaction. The simulated carbon black aggregate was then removed from the simulation to mimic the voids left behind in the experimentally reconstructed three-dimensional electrodes.

To calculate the active material tortuosity,  $\tau_o$ , a finite element model was implemented to define the average transport properties. The macroscopic diffusivity was calculated through Fick's first law. The diffusion flux was obtained by integrating the concentration gradient across the thickness of the domain. In agreement with previous work [21], the size of the simulated domain was set to be larger than  $100 \mu\text{m}$ , in order to eliminate any extraneous surface effects. (See figure 8 of the appendix for further details.) Following the analytical description of battery tortuosity by Vijayaraghavan *et al* [21], the inactive material tortuosity,  $\tau_v$ , of an electrode is approximated using the Bruggeman relation,  $\tau_v = \epsilon_v^{-1/2}$ .

The described method was implemented in Batts3D [40], a set of Python-based software libraries developed specifically to simulate the charge transport in rechargeable batteries with complex three-dimensional microstructures. The relative tolerance of convergence was set to  $1 \times 10^{-6}$ . Simulations took on the order of 4 h of wall time on an eight core, 2.4 GHz Linux Ubuntu 10.04 computer with 128 GB of random access memory (RAM). On the order of 40 GB of RAM were used in each calculation.

### 4. Trends in tortuosity with electrode processing

While the different amounts of inactive material and compaction strength change the porosity, there is a corresponding change in the tortuosity. Figure 2 shows that the active material tortuosities plotted against the porosity of all 16 different experimental electrodes closely

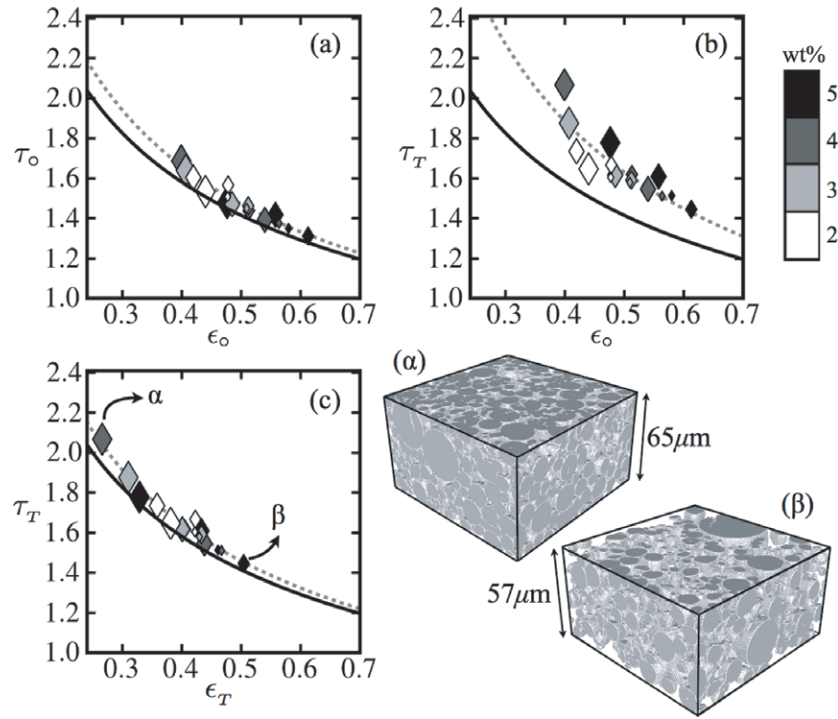


**Figure 2.** (a) Active material tortuosity,  $\tau_o$ , (b) total tortuosity,  $\tau_T$ , as a function of active material porosity,  $\epsilon_o$ , and (c) total tortuosity,  $\tau_T$ , as a function of total porosity,  $\epsilon_T$ . The marker size is modulated with respect to the intensity of the compaction stress value,  $P$ : 0, 0.3, 0.6 and 2 kbar. The grayscale embodies the amount of carbon additive,  $f_v$ . The solid lines correspond to the Bruggeman estimate. The active phase tortuosity follows a  $\tau_o = 1.01/\epsilon_o^{0.54}$  relationship and  $\tau_T = 1.01/\epsilon_T^{0.53}$  relation. Insets show the microstructures with the highest,  $\alpha$ , and the lowest,  $\beta$ , tortuosity.

follow the Bruggeman relation (indicated by black lines) but consistently lie above it. (Alternate descriptions of tortuosity as a function of carbon black and compaction can be found in figures 9 and 10 of the [appendix](#).)

Figure 2(b) shows the total tortuosity as a function of active phase porosity. This plot acts as a design guideline since the energy density of a battery is the energy density of the active material times  $1 - \epsilon$ , but the power density is governed by the tortuosity induced ohmic losses [41, 42], particularly for high power density applications. Here, the solid line allows the validity of the Bruggeman relationship to be assessed, for porosity and tortuosity stemming from the underlying phases (figures 2(a) and (c)). To understand why all the experimental microstructures follow the Bruggeman estimate but lie above it, we turn to numerical simulations.

Computer-generated electrodes using experimental particle size distributions and compaction strengths equivalent to the experimental samples are simulated. Figure 3 shows the tortuosity versus porosity values for electrodes with a lognormal size distribution. These electrodes exhibit Bruggeman type behavior, as do samples with a Gaussian particle size distribution, in agreement with Vijayaraghavan *et al* [21]. However, unlike the experimental samples, which show tortuosity above the Bruggeman relation, electrodes with both Gaussian and lognormal particle size distributions exhibit sub-Bruggeman tortuosity.



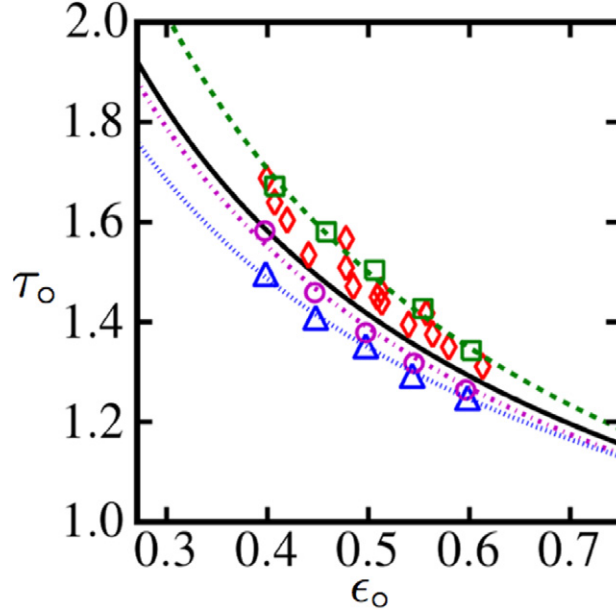


**Figure 3.** Comparison of active material tortuosity,  $\tau_0$ , for computer-generated and experimentally determined electrodes.  $\diamond$  correspond to experimental electrodes,  $\circ$  to electrodes with a Gaussian particle size distribution,  $\tau_0 = 0.98/\epsilon_0^{1/2}$ ,  $\triangle$  to electrodes with lognormal particle size distribution,  $\tau_0 = 1/\epsilon_0^{0.44}$  and  $\square$  to electrodes with packing inhomogeneities,  $\tau_0 = 1/\epsilon_0^{0.58}$ .

To understand why the tortuosities of the simulated electrodes with the same particle size distribution as our experimental electrode are consistently lower than the tortuosity found in the experimental data, we consider that the tomography data (figure 1) show evidence of porosity inhomogeneities. The incorporation of porosity clusters into the simulated electrodes enables excellent agreement with the tortuosities determined from the experimental electrodes. Therefore, inhomogeneities in particle packing result in a tortuosity increase of approximately 13–16% with respect to a uniformly packed electrode, in the limit of perfectly spherical particles. Spatial inhomogeneities in the active material distribution are also known to induce local lithium accumulation and depletion, which in turn directly controls the macroscopic galvanostatic efficiency [42].

### 5. Effect of particle polydispersity and electrode inhomogeneity

In addition to electrode inhomogeneity, the particle size distribution also plays an important role in the porous electrode microstructure. However, since specific distributions are challenging to produce experimentally, simulated electrodes are used to probe the effect of particle size dispersion.

In order to analyze the effect of particle size polydispersity and electrode inhomogeneity on tortuosity, we first define a metric,  $\chi$ , to quantify the degree of crystallinity in an electrode:

$$\chi = \frac{\text{CN}_i(1 - (\sigma_i/\sigma_{\max}))}{12}, \quad (5)$$

where  $\sigma_i = \sqrt{\sum_{j=1}^{\text{CN}_i} (r_i - r_j)^2 / \text{CN}_i}$  is the local polydispersity of the  $i$ th particle and  $\sigma_{\max}$  is the maximum local polydispersity of the electrode.  $r_i$  is the radius of the  $i$ th particle,  $r_j$  is the

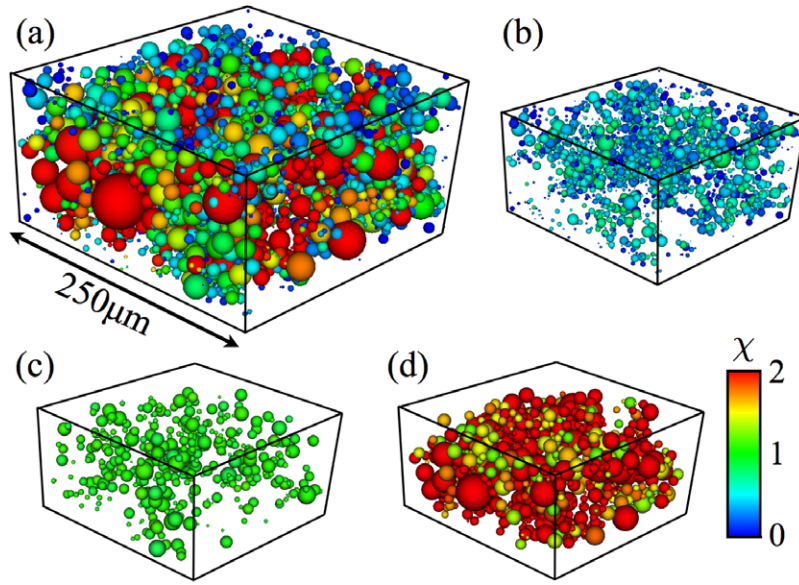


**Figure 4.** Position-dependent degree of crystallinity,  $\chi$ , for three-dimensionally reconstructed experimental electrode,  $P = 2$  kbar,  $f_v = 2$  wt%, and  $\epsilon_o = 0.44$ . (a) shows the entire section, (b) shows particles with  $\chi < 0.9$ , (c) shows particles in the  $0.9 \leq \chi \leq 1.1$  range and (d) shows particles with  $\chi > 1.1$ . Calculations demonstrate the absence of particle ordering (crystallinity) in the electrode.

radius of the  $j$ th nearest neighbor and  $CN_i$  is the coordination number of the  $i$ th particle. Here, the coordination number,  $CN_i$ , is defined based on a volumetric approach. Particles within a spherical vicinity from  $i$ th particle to the center of its largest contact neighbor are considered to be the nearest neighbors.

Equation (5) provides a measure of the local degree of ordering that a perfectly spherical, particle-based electrode would deliver. In the limit of a monodisperse particle distribution,  $\sigma_r = 0$ , that displays crystalline ordered arrangements of particles,  $CN_i = 12$ , the degree of crystallinity will have a unit value,  $\chi = 1$ . Similarly, deviations from unity will highlight local richness of vacancies,  $\chi < 1$ , or particle clustering,  $\chi > 1$ .

We applied this analysis to the experimental samples. Figure 4 illustrates that the spatial configuration of particles is highly nonuniform. Low  $\chi$  values correlate with particles in the vicinity of internal open porosity or close to the top or bottom surfaces, and very large  $\chi$  values correlate with clusters of large particles surrounded by very small ones. Results demonstrate that long-range ordering (crystallinity) is not present in the experimental samples, since no local periodicity is visually apparent (see figure 4(c)). Here, particles whose crystallinity index is  $\chi = 1$  have 12 nearest neighbors and comparable size, but those neighbors do not share the same degree of crystallinity. Hence, no region exhibits the necessary periodicity to form a statistically representative crystalline cluster or unit cell.

Figure 5 assesses the effect of particle polydispersity on the degree of ordering using computer-generated microstructures. For electrodes with a degree of polydispersity greater than  $\sigma_r = 0.4\bar{r}$  and an active material porosity greater than  $\epsilon_o = 0.4$ , the system will display poor particle ordering. However, although the use of monodisperse particles favors the formation of ordered arrangements, particle interactions prevent the electrode from crystallizing. Specifically, figure 5(a) shows that over 40% of electrode material exhibits low crystallinity,  $\chi < 0.9$ , due to packing defects. Only a small amount of polydispersity is



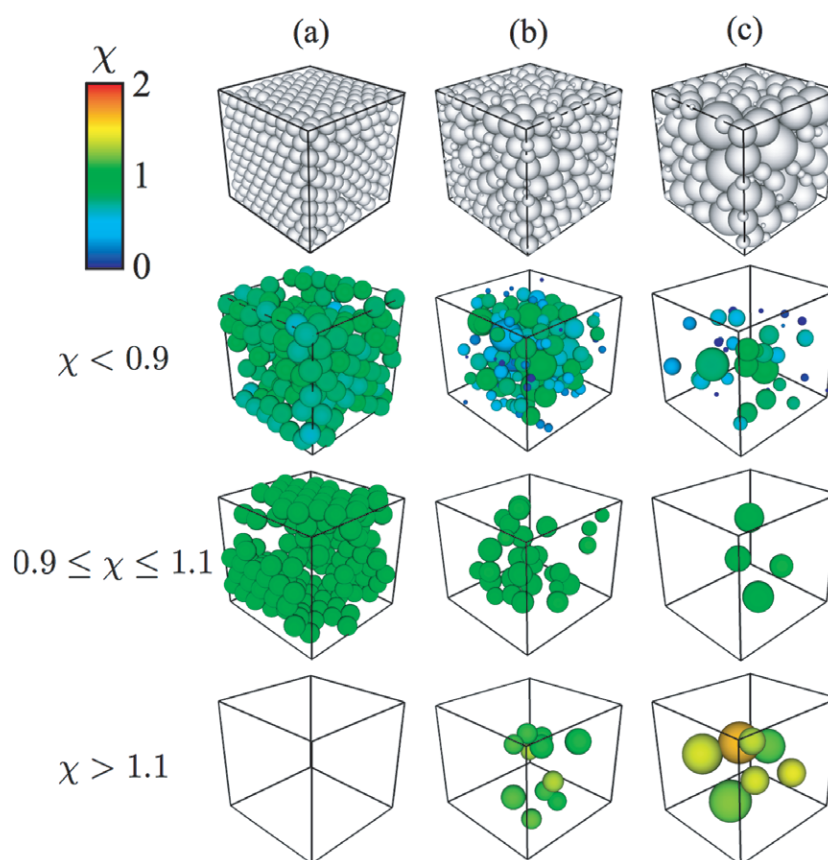


**Figure 5.** Spatial distribution of degree of crystallinity,  $\chi$ , for electrodes displaying different degrees of polydispersity: (a)  $\sigma_r = 0$ , (b)  $\sigma_r = 0.4\bar{r}$  and (c)  $\sigma_r = \bar{r}$ . The degree of crystallinity decreases as the polydispersity increases as demonstrated by the decreased crystallinity fraction. In all samples, the porosity is fixed, i.e.  $\epsilon_o = 0.27$ .

necessary to cause unfavorable conditions for ordering and results in a random structure (see figures 11 and 12 in the [appendix](#) for further details).

Figure 6 summarizes the tortuosities for the different particle size distributions and packings. Perfectly ordered particle architectures, such as face center cubic, body center cubic, hexagonal close packed and simple hexagonal, show values of tortuosity up to 10% lower with respect to those predicted by the Bruggeman relation. In particular, simple hexagonal delivers directional tortuosity within 2% of the Hashin–Shtrikman lower bound [29, 30, 32]. Low porosity architectures, such as those formed from particles with a Gaussian size distribution, show that when an inactive component such as carbon black is present, the total tortuosity,  $\tau_T$ , increases because the transport in the remaining pore space is constrained by carbon black. Spatial inhomogeneities, as described by the simulated clustered arrangements, result in electrodes with higher tortuosities, consistent with the experimental electrodes.

Figure 7 summarizes the normalized exposed area of electrochemically active material per unit volume,  $a\bar{r}$ , for electrodes of different degrees of polydispersity. For a Gaussian size distribution, the highest area density is achieved by employing a monodisperse spherical particle population. The area density limit is described by equation (2). However, in the

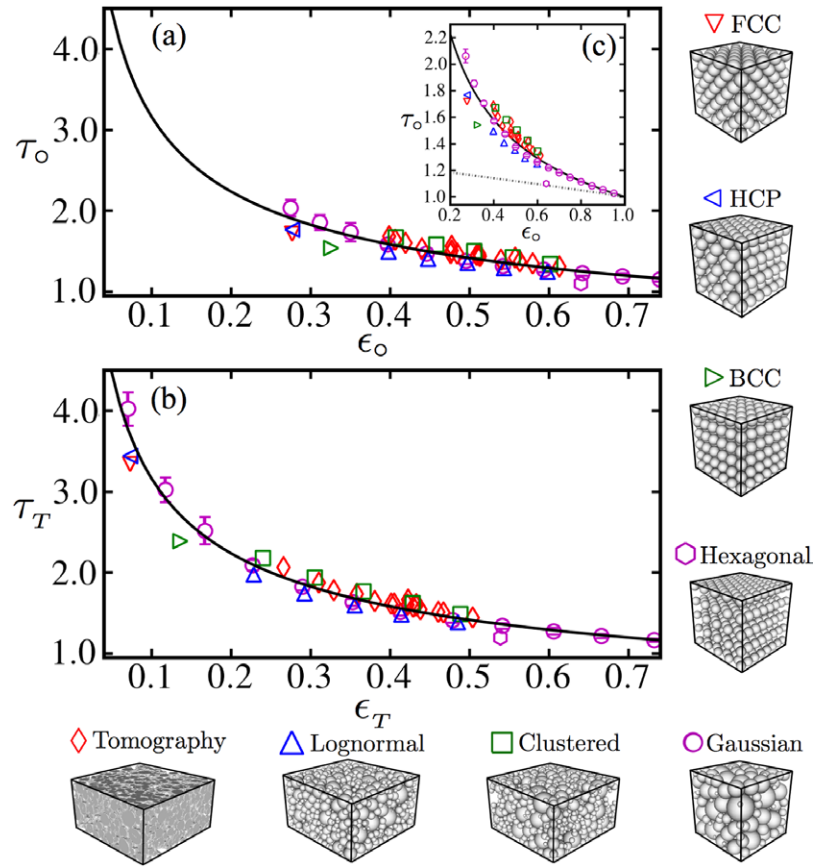


**Figure 6.** (a) Active phase tortuosity,  $\tau_o$ , as a function of active material porosity,  $\epsilon_o$ , and (b) total tortuosity,  $\tau_T$ , as a function of total electrode porosity,  $\epsilon_T$ , for analyzed architectures (satellite insets). Inset (c) delineates the tortuosity deviations from the Bruggeman ideal (solid line) and the Hashin–Shtrikman lower bound (dashed–dotted line).

limit of crystalline packed, perfectly spherical particles, the highest area density achievable corresponds to the crystalline close packed porosity,  $\epsilon_o = 1 - \pi/3\sqrt{2} \approx 0.27$  for face center cubic and hexagonal close packed structures. Results show that if  $\sigma_r \leq 0.2\bar{r}$ , the area density corresponds to the theoretical limit within 10% deviation. As the polydispersity increases beyond  $\sigma_r = 0.2\bar{r}$ , the area density decreases rapidly to one third of the monodisperse value. This suggests that moderate control of polydispersity provides an improvement in instantaneous power density that would be greatly beneficial, particularly for applications that demand sudden energy pulses.

In practice, by introducing surface roughness to the particles, electrodes could achieve higher area densities, i.e.,  $a\bar{r} = 3S_A(1 - \epsilon_o)$ , where  $S_A$  is the representative surface roughness per particle. For perfectly smooth surfaces,  $S_A = 1$ , and as the particle roughness increases,  $S_A > 1$ , the area density increases for fixed particle size polydispersity. Therefore, while the results presented herein for perfectly spherical particles would be a lower bound of the local reactivity of a porous electrode with an appreciable degree of surface roughness, they highlight the expected effect of polydispersity and particle packing on the power density of the electrode layer. Furthermore, electrodes displaying a segregated lognormal particle size

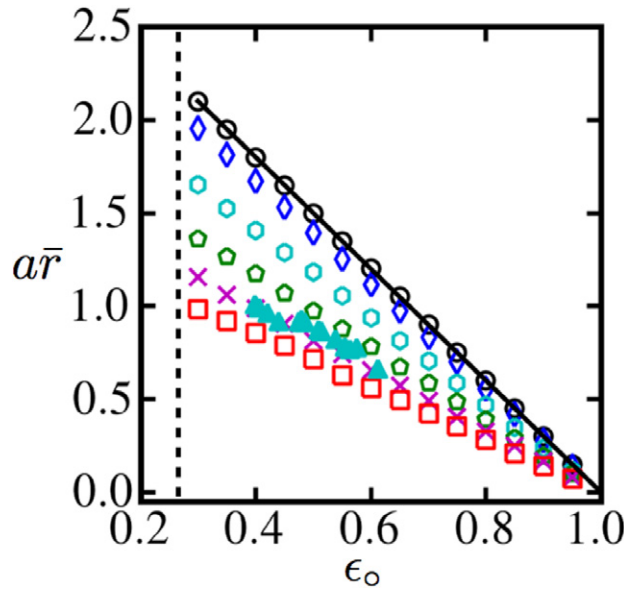


**Figure 7.** Normalized active area per unit volume as a function of active phase porosity.  $\circ$  correspond to monodisperse, randomly distributed electrode particles.  $\diamond$  corresponds to  $\sigma_r = 0.2\bar{r}$ ,  $\circ$  to  $\sigma_r = 0.4\bar{r}$ ,  $\hexagon$  to  $\sigma_r = 0.6\bar{r}$ ,  $\times$  to  $\sigma_r = 0.8\bar{r}$  and  $\square$  to  $\sigma_r = \bar{r}$ .  $\triangle$  corresponds to electrodes with a lognormal particle size distribution with the same degree of polydispersity as displayed by  $\circ$  and the experimental samples. The solid line is the reaction area density limit as described by equation (2). The dashed line corresponds to  $\epsilon_o = 1 - \pi/3\sqrt{2} \approx 0.27$ , the crystal packing limit.

distribution show lower area density compared with electrodes displaying the corresponding Gaussian, spatially uniform, distribution of particles due to its skewness toward a larger particle size.

## 6. Summary and conclusions

We calculated and analyzed the battery tortuosity from three-dimensional reconstructions of experimental porous electrodes, obtained using synchrotron x-ray tomography and computer-generated electrodes in order to determine potential approaches to decrease tortuosity while still using traditional porous electrode manufacturing.

We found that independent of the amount of inactive additive or compaction strength, all experimental electrodes exhibit total tortuosities,  $\tau_T$ , as a function of total porosities,  $\epsilon_T$ , that follow the Bruggeman relation. The spatial inhomogeneities in the experimental electrodes increases the total tortuosity by approximately 15% as compared with electrodes fabricated from the same particle size distribution with a uniform spatial distribution. In addition, clustering, polydispersity and segregation of particles reduce the local reactivity of the analyzed experimental electrodes.

This work highlights two paths for reducing tortuosity and improving reactive area in traditionally manufactured porous electrodes. Spherical particles with polydispersity of  $\sigma_r < 0.4\bar{r}$  are already commercially available. Using these particles in the manufacture of a highly homogeneous electrode would enable a tortuosity reduction of 5–10% lower than the Bruggeman ideal. Alternatively, while organized periodic structures of monodisperse particles result in the lowest tortuosity values, reducing the particle size distribution to have a

standard deviations of  $\sigma_r \leq 0.2\bar{r}$  would achieve tortuosity values within 10% of the perfectly ordered structure. In addition, this controlled polydispersity results in an electrochemical response within 10% of that delivered by a monodisperse electrode, thus enabling the practical maximization of the instantaneous power density. Manufacturing more homogeneous electrodes and improving monodispersity of active particles both come at higher manufacturing costs, and the relative benefits of each approach must be assessed for the particular active material and electrode application.

### Acknowledgments

DWC and REG thank the National Science Foundation CMMI 0856491 for financial support and Professor Yet-Ming Chiang, Professor Martin Bazant and Dr Stephen Harris for useful discussions. ME and VW thank Professors Petr Novak, David Norris and Rudolf von Rohr for experimental support. The tomography experiments were performed on the TOMCAT beamline at the Swiss Light Source, Paul Scherrer Institut, Villigen, Switzerland.

### Appendix.

Figure 9 summarizes the effect of the weight fraction of carbon additives,  $f_v$ , on the macroscopic tortuosity for fixed compaction stress,  $P$ . Results demonstrate that for only lightly compressed electrodes, a higher weight fraction of additives tends to decrease active material tortuosity because the average spacing between particles of active material increases. However, the addition of carbon black for the highest compaction ( $P = 2$  kbar) causes an increase in the tortuosity of the system. In this case, the compression is likely sufficient to overcome the

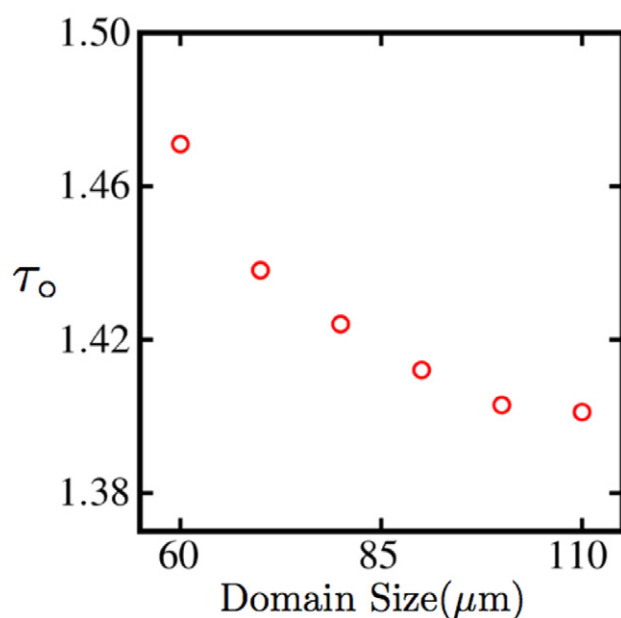


**Figure 8.** Active material tortuosity as a function of simulation domain size. The calculation demonstrates that the calculated tortuosity of porous electrodes is simulation domain size independent for systems larger than 100 μm.

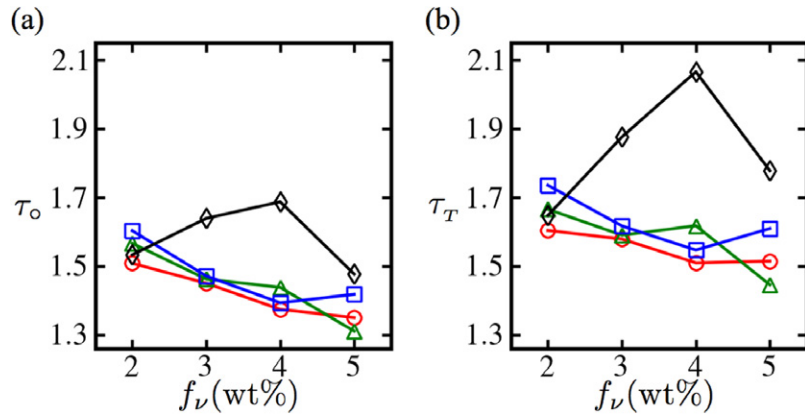


**Figure 9.** (a) Active material tortuosity,  $\tau_o$ , and (b) total tortuosity,  $\tau_T$ , as a function of wt% carbon black,  $f_v$ , in the electrode.  $\circ$  correspond to uncompressed electrodes,  $\triangle$  to 0.3 kbar compaction,  $\square$  to 0.6 kbar compaction, and  $\diamond$  to 2 kbar compaction. Calculations on experimentally reconstructed microstructures demonstrate the effect of the different components on the overall tortuosity.

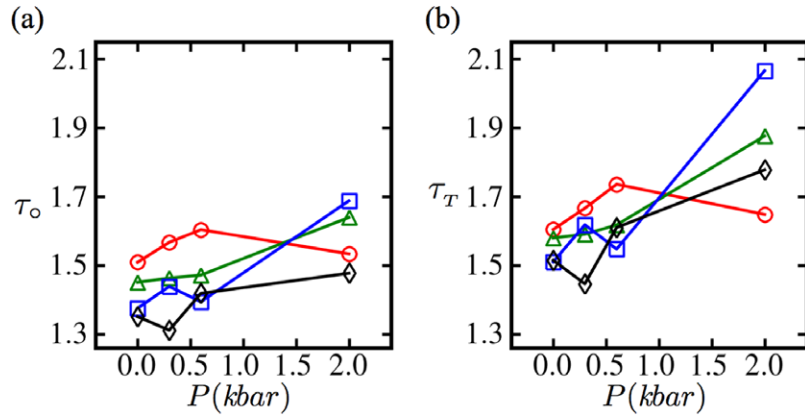
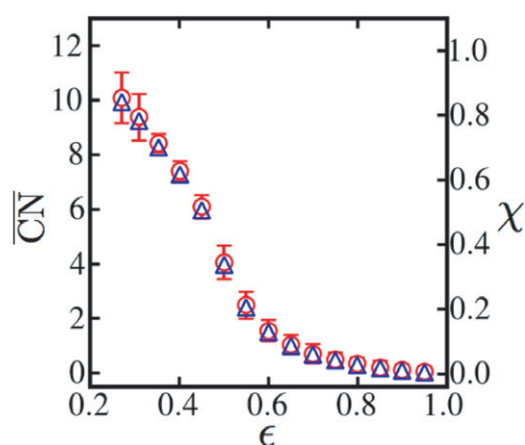


**Figure 10.** (a) Active material tortuosity,  $\tau_o$ , and (b) total tortuosity,  $\tau_T$ , as a function of electrode compaction stress.  $\circ$  correspond to electrodes with 2 wt%,  $\triangle$  to 3 wt%,  $\square$  to 4 wt% and  $\diamond$  to 5 wt%.

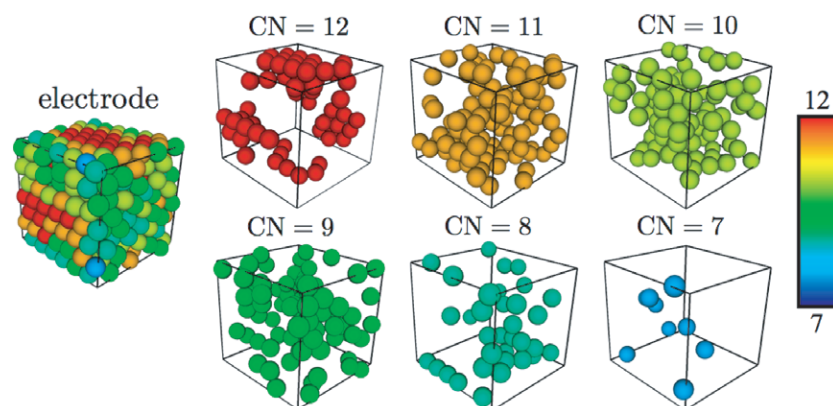
repulsive forces from nanoscale carbon and cause the active particles to sit closer together. However, a reversal of this trend is observed at  $f_v \geq 4$  wt%. Such a maximum suggests a structural transition where particle rearrangement, perhaps lubricated by the additional carbon black, leads to a rapid decrease in tortuosity [43–45].

Figure 10 demonstrates that tortuosity is dependent on compaction stress due to the decreasing availability of interstitial space. Specifically, electrodes with  $f_v = 2$  wt% exhibit a maximum tortuosity at  $P = 0.6$  kbar, further supporting the possibility of a compaction induced structural transition. Beyond  $P = 0.6$  kbar, particle rearrangement and tortuosity minimization is observed [46, 47].

Figure 11 shows the average coordination number,  $\overline{CN}$ , of electrodes as a function of porosity for a particle size polydispersity of  $\sigma_r = 0$ . As porosity decreases, the coordination number increases.  $\epsilon_o \approx 0.4$  highlights the onset of crystallinity.



**Figure 11.** Average coordination number (○) and crystallinity (△) as a function of porosity for a particle size polydispersity of  $\sigma_r = 0$ .



**Figure 12.** Local coordination number, CN, for a monodisperse electrode. Clustered particles with CN = 12 are ordered.

## References

- [1] Vu A, Qian Y and Stein A 2012 Porous electrode materials for lithium-ion batteries—how to prepare them and what makes them special *Adv. Energy Mater.* **2** 1056
- [2] Doyle C M 1995 Design and simulation of lithium rechargeable batteries *PhD Thesis* University of California at Berkeley, Berkeley, CA
- [3] Fuller T M, Doyle M and Newman J 1994 Simulation and optimization of the dual lithium ion insertion cell *J. Electrochem. Soc.* **141** 1
- [4] Arora P, Doyle M and White R E 1999 Mathematical modeling of the lithium deposition overcharge reaction in lithium-ion batteries using carbon-based negative electrodes *J. Electrochem. Soc.* **146** 3543
- [5] Darling R and Newman J 1997 On the short-time behavior of porous intercalation electrodes *J. Electrochem. Soc.* **144** 3057
- [6] Hellweg H 2000 Microstructural modeling of lithium battery electrodes *MS Thesis* Massachusetts Institute of Technology, Cambridge, MA
- [7] Gu W B and Wang C Y 2000 Thermal–electrochemical modeling of battery systems *J. Electrochem. Soc.* **147** 2910
- [8] Gu W B and Wang C Y 2000 Computational fluid dynamics modeling of a lithium/thionyl chloride battery with electrolyte flow *J. Electrochem. Soc.* **147** 427



- [9] Rao L and Newman J 1997 Heat-generation rate and general energy balance for insertion battery systems *J. Electrochem. Soc.* **144** 2697
- [10] Song L and Evans J W 2000 Electrochemical–thermal model of lithium polymer batteries *J. Electrochem. Soc.* **147** 2086
- [11] Thomas K E and Newman J 2003 Thermal modeling of porous insertion electrodes *J. Electrochem. Soc.* **150** A176
- [12] Botte G G, Subramanian V R and White R E 2000 Mathematical modeling of secondary lithium batteries *Electrochim. Acta* **45** 2595
- [13] Botte G G and White R E 2001 Modeling lithium intercalation in a porous carbon electrode *J. Electrochem. Soc.* **148** A54
- [14] Zhang H, Yu X and Braun P V 2011 Three-dimensional bicontinuous ultrafast-charge and -discharge bulk battery electrodes *Nature Nanotechnol.* **6** 277
- [15] Stephenson D E, Hartman E M, Harb J N and Wheeler D R 2007 Modeling of particle–particle interactions in porous cathodes for lithium-ion batteries *J. Electrochem. Soc.* **154** A1146
- [16] Long J W, Dunn B, Rolison D R and White H S 2004 Three-dimensional battery architectures *Chem. Rev.* **104** 4463
- [17] Sakamoto J S and Dunn B 2002 Hierarchical battery electrodes based on inverted opal structures *J. Mater. Chem.* **12** 2859
- [18] Thorat I V, Stephenson D E, Zacharias N A, Zaghbi K, Harb J N and Wheeler D R 2009 Quantifying tortuosity in porous Li-ion battery materials *J. Power Sources* **188** 592
- [19] Stephenson D E, Walker B C, Skelton C B, Gorzkowski E P, Rowenhorst D J and Wheeler D R 2011 Modeling 3D microstructure and ion transport in porous Li-ion battery electrodes *J. Electrochem. Soc.* **158** A718
- [20] Kehrwald D, Shearing P R, Brandon N P, Sinha P K and Harris S J 2011 Local tortuosity inhomogeneities in a lithium battery composite electrode *J. Electrochem. Soc.* **158** A1393
- [21] Vijayaraghavan B, Ely D R, Chiang Y-M, García-García R and García R E 2012 An analytical method to determine tortuosity in rechargeable battery electrodes *J. Electrochem. Soc.* **159** A548
- [22] Petersen E E 1958 Diffusion in a pore of varying cross section *AIChE J.* **4** 343
- [23] Sherwood T G, Pigford R L and Wilke C R 1975 *Mass Transfer* (New York: McGraw-Hill) pp 39–43
- [24] Shen L and Chen Z 2007 Critical review of the impact of tortuosity on diffusion *Chem. Eng. Sci.* **62** 3748
- [25] Bruggeman D A 1935 Berechnung Verschiedener Physikalischer Konstanten von Heterogenen Substanzen. *Ann. Phys., Lpz.* **24** 636
- [26] Djian D, Alloin D, Martinet S, Lignier H and Sanchez J Y 2007 Lithium-ion batteries with high charge rate capacity: influence of the porous separator *J. Power Sources* **172** 416
- [27] Doyle M, Newman J, Gozdz A S, Schmutz C N and Tarascon J-M 1996 Comparison of modeling predictions with experimental data from plastic lithium ion cells *J. Electrochem. Soc.* **143** 1890
- [28] Abraham K M 1993 Directions in secondary lithium battery research and development *Electrochim. Acta* **38** 1233
- [29] Ferguson T R and Bazant M Z 2012 Nonequilibrium thermodynamics of porous electrodes *J. Electrochem. Soc.* **159** A1967
- [30] Torquato S and Haslach H W Jr 2002 Random heterogeneous materials—microstructure and macroscopic properties *Appl. Mech. Rev.* **55** B62–3
- [31] Wiener O 1912 Die Theorie des Mischkörpers für das Feld des stationären Stromung *Abh. Math.-Physischen Klasse Königl. Sächs. Gesel. Wissen* **32** 509
- [32] Hashin Z and Shtrikman S 1962 A variational approach to the theory of the effective magnetic permeability of multiphase materials *J. Appl. Phys.* **33** 3125
- [33] Shearing P R, Howard L E, Jorgensen P S, Brandon N P and Harris S J 2010 Characterization of the 3-dimensional microstructure of a graphite negative electrode from a Li-ion battery *Electrochem. Commun.* **12** 374
- [34] Gupta A, Seo J H, Zhang X, Du W, Sastry A M and Shyy W 2011 Effective transport properties of LiMn<sub>2</sub>O<sub>4</sub> electrode via particle-scale modeling *J. Electrochem. Soc.* **158** A487
- [35] Patel K K, Paulsen J M and Desilvestro J 2003 Numerical simulation of porous networks in relation to battery electrodes and separators *J. Power Sources* **122** 144
- [36] Newton M R, Morey K A, Zhang Y, Snow R J, Diwekar M, Shi J and White H S 2004 Anisotropic diffusion in face-centered cubic opals *Nano Lett.* **4** 875
- [37] Zacharias N A, Nevers D R, Skelton C, Knackstedt K, Stephenson D E and Wheeler D R 2013 Direct measurements of effective ionic transport in porous Li-ion electrodes *J. Electrochem. Soc.* **160** A306
- [38] Ebner M, Geldmacher F, Marone F, Stampanoni M and Wood V 2013 X-ray tomography of porous, transition metal oxide based lithium ion battery electrodes *Adv. Energy Mater.* **3** 201200932
- [39] Abe S, Altinay C, Boros V, Hancock W, Latham S, Mora P, Place D, Petterson W, Wang Y and Weatherley D 2009 *ESyS-Particle: HPC Discrete Element Modeling Software* (Open Software License version 3.0)

- [40] Vijayaraghavan B, García R E and Chiang Y-M 2011 Microstructure modeling of rechargeable lithium-ion batteries *B5—Microstructure, Mechanisms, and Modeling of Battery Materials 219th ECS Meeting (Montreal, QC, Canada, 1–6 May 2011)* (MA2011-01)
- [41] Newman J 1995 Optimization of porosity and thickness of a battery electrode by means of a reaction-zone model *J. Electrochem. Soc.* **142** 97
- [42] Smith M, García R E and Horn Q C 2009 The effect of microstructure on the galvanostatic discharge of graphite anode electrodes in LiCoO<sub>2</sub>-based rocking-chair rechargeable batteries *J. Electrochem. Soc.* **156** A896
- [43] Srebro Y and Levine D 2003 Role of friction in compaction and segregation of granular materials *Phys. Rev. E* **68** 061301
- [44] Cantelaube F and Bideau D 1995 Radial segregation in a 2D drum: an experimental analysis *Europhys. Lett.* **30** 133
- [45] Shinbrot T and Muzzio F J 1998 Reverse buoyancy in shaken granular beds *Phys. Rev. Lett.* **81** 4365
- [46] Martin C L, Bouvard D and Shima S 2003 Study of particle rearrangement during powder compaction by the discrete element method *J. Mech. Phys. Solids* **51** 667
- [47] Liu J and De Lo D P 2001 Particle rearrangement during powder compaction *Metall. Mater. Trans. A* **32A** 3117
- [48] Hinds W C 1999 *Aerosol Technology: Properties, Behavior, and Measurement of Airborne Particles* (New York: Wiley-Interscience)
- [49] García R E, Chiang Y-M, Carter W C, Limthongkul P and Bishop C M 2005 Microstructural modeling and design of rechargeable lithium-ion batteries *J. Electrochem. Soc.* **152** A255
- [50] Qu M, Woodford W H, Maloney J M, Carter C W, Chiang Y-M and Van Vliet K J 2012 Nanomechanical quantification of elastic, plastic, and fracture properties of LiCoO<sub>2</sub> *Adv. Energy Mater.* **2** 940